A Mechanical, Microstructural, and Damage Study of Various Tailor Hot Stamped Material Conditions Consisting of Martensite, Bainite, Ferrite, and Pearlite

ALEXANDER BARDELCIK, CARYN J. VOWLES, and MICHAEL J. WORSWICK

This paper examines the mechanical, microstructural, and damage characteristics of five different material conditions that were created using the tailored hot stamping process with in-die heating. The tailored material conditions, TMC1 to TMC5 (softest-hardest), were created using die temperatures ranging from 700 °C to 400 °C, respectively. The tensile strength (and total elongation) ranged from 615 MPa (0.24) for TMC1 to 1122 MPa (0.11) for TMC5. TMC3 and TMC4 exhibited intermediate strength levels, with almost no increase in total elongation relative to TMC5. FE-SEM microscopy was used to quantify the mixed-phase microstructures, which ranged in volume fractions of ferrite, pearlite, bainite, and martensite. High-resolution optical microscopy was used to quantify void accumulation and showed that the total void area fraction at ~ 0.60 thickness strain was low for TMC1 and TMC5 (~ 0.09 pct) and highest for TMC3 (0.31 pct). Damage modes were characterized and revealed that the poor damage behavior of TMC3 (martensite/bainite/ferrite composition) was a result of small martensitic grains forming at grain boundaries and grain boundary junctions, which facilitated void nucleation as shown by the highest measured void density for this particular material condition. The excellent ductility of TMC1 was a result of a large grained ferritic/pearlitic microstructure that was less susceptible to void nucleation and growth. Large titanium nitride (TiN) inclusions were observed in all of the tailored material conditions and it was shown that they noticeably contributed to the total void accumulation, specifically for the TMC3 and TMC4 material conditions.

I. INTRODUCTION

HOT stamping (or press hardening) is now a mature and established technology which allows the forming of ultra high-strength steel (UHSS) automotive structural components that are both lightweight and meet the demands of passenger protection during crash. These properties are due to a solid-state phase transformation during the forming process, in which a fully austenitized blank is simultaneously formed and quenched (at cooling rates > ~ 27 °C/s) within the tool, resulting in a fully martensitic as-formed microstructure which exhibits a tensile strength and total elongation of ~ 1500 MPa and ~ 0.10 strain, respectively.[1] Although conventionally hot stamped structural components possess excellent intrusion resistance characteristics, the overall crashworthiness of these parts stands to benefit from regions of lower strength and greater ductility for improved energy absorption.[2] This has led to the development of tailored hot stamping technologies, which are used to produce hot stamped parts with local regions consisting of lower strength and more ductile microstructures. Tailored hot stampings can be manufactured using a number of different processing routes, as reviewed in depth by Merklein et al.[3] Of these tailoring processes, the in-die heating (or heated tool) process relies on heating a section of the stamping die where tailored properties are desired. During the hot stamping process, the heated tooling section(s) within the die forces the cooling rate below 27 °C/s as the part is quenched to the heated tool temperature. When the part is released from the die, the heated region further cools (slowly) due to convection.[4] Recently, this tailoring process has been applied to introduce soft zones

ALEXANDER BARDELCIK and CARYN J. VOWLES are with the University of Guelph, School of Engineering, 50 Stone Road East, Guelph, ON N1G 2W1, Canada. Contact e-mail: abardelc@uoguelph.ca MICHAEL J. WORSWICK is with the University of Waterloo, Department of Mechanical and Mechatronics Engineering, 200 University Avenue West, Waterloo, ON N2L 3G1, Canada.

within the hot stamped rear frame member of the 2016 Honda Civic for optimized impact performance.[5]

The tensile behavior of hot stamped and tailored microstructures has been investigated by multiple researchers, all of which studied Al-Si coated boron alloyed 22MnB5 hot stamping steel (Usibor® 1500-AS). Bardelcik et al.[6,7] austenized and quenched boron steel specimens with compressed air to produce tailored microstructures (> 268 HV) and develop a strain rate-sensitive constitutive model. Barcelona and Palmeri,[8] Min et al.[9] and Bardelcik et al.[10] all used a Gleeble thermal-mechanical simulator to simultaneously quench and deform boron steel at sub-critical cooling rates (< 27 °C/s) and showed that deformation facilitated the decomposition of austenite into bainite and ferrite at cooling rates that would typically suppress these transformations in the absence of deformation. Utilizing a heated die, Golling et al.[11] created tailored microstructures by enforcing isothermal phase transformations. Sirthananan et al.[12] created tailored microstructures consisting of martensite and bainite only, by isothermally holding the specimens at different constant temperatures for up to 120 seconds.

Although the above-mentioned studies focus on tailored microstructures created in a laboratory, the experiments do not simulate the production-scale thermal-mechanical boundary conditions operative in hot stamping with in-die heating. Due to the complex boundary conditions (isothermal/non-isothermal cooling, deformation, die contact, conductive and convective cooling, etc.), the as-formed microstructures of production-scale hot stamped parts are most likely different from those created at a coupon scale. A number of researchers have developed near production-scale hot stamping (with in-die heating) experiments, but have limited their in-die heating temperature to a maximum of 500 °C and long hold times that are not practical for implementation on a production-scale due to cycle time requirements.[4,13–15] These studies rely on optical microscopy to characterize the tailored microstructures (some SEM work in Reference 15) and do not relate the effect of microstructural composition (multi-phase volume fractions, morphology, etc.) to the mechanical and damage behavior of the tailored materials. Although there have been phenomenological fracture models developed for tailored hot stampings,[15–17] damage characterization (void accumulation, multi-phase interaction, etc.) was not considered in these studies.

The combined work of Prajogo[18] and Omer et al.[19] resulted in the development of a near production-scale hot stamping process, which utilized in-die heating at temperatures up to 700 °C. In their work, a 500 mm hat-section channel was hot stamped with tailored properties, but only the hardness of the resulting tailored microstructures was assessed with limited microstructural characterization. The current work focuses on measuring the macro-scale tensile behavior of multiple tailored material conditions (created in References 18, 19) that span the range of hardness from 193 to 486 HV$_{1000}$. After the tensile testing, a detailed microstructural analysis was conducted to characterize the morphology and distribution of these multi-phase tailored material conditions. The effect of these multi-phase microstructures on damage evolution during plastic deformation was then quantified and linked to the observed macro behavior.

II. EXPERIMENTAL METHODS

A. Hot Stamping Material

A 22MnB5 boron alloyed Al-Si coated steel sheet metal (ArcelorMittal, Usibor® 1500-AS) with a nominal thickness of 1.2 and 1.8 mm, was used in this work. The as-received microstructure of the steel consists of ferrite/pearlite with a yield strength and ultimate tensile strength of ~ 485 and ~ 612 MPa, respectively. The chemical composition of the steel is given in Table I.

B. Hot Stamping Experiments and Tailored Material Conditions

Tailored hot stamping of a 3-Point Bend and Axial hat-section rail were developed in References 18 and 19, respectively. The geometry of the parts and locations of the tailored regions are shown in Figure 1. A brief description of the hot stamping experiments is provided here, while a detailed description can be found in References 18 and 19. As a result of a large-scale study involving the two different rail configurations, forty different tailored microstructures were created by varying the following production-scale process parameters:

- Die temperature—25 °C, 400 °C, 600 °C, and 700 °C
- Quench time—4 and 10 seconds
- Material thickness—1.2 and 1.8 mm

As a result of this large-scale study, the hardness of the forty different tailored microstructures was characterized to show the range in tailored properties that can be achieved using the in-die heating tailoring process. The purpose of the current work is to conduct an in-depth tensile, microstructural, and damage analysis of five (of the forty) Tailored Material Conditions (referred to as TMC1 to TMC5) that span the entire range of as-formed tailored material conditions from softest to hardest. A fully hardened material condition was also examined and is referred to as MART. The different tailored material conditions examined in this work were produced by varying the die temperature,

Table I. Chemical Composition (Wt Pct) of the Usibor® 1500-AS Steel Used in this Work

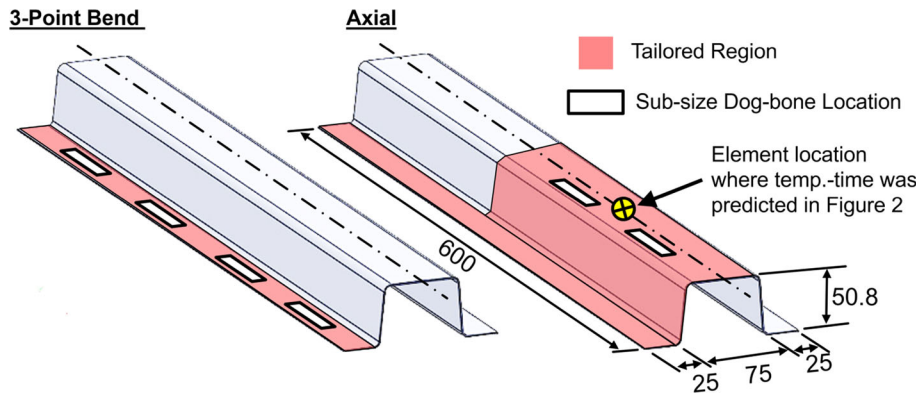| C	Mn	B	Si	P	Cu	Ni	Cr	Al	Ti	Mo
0.22	1.23	0.004	0.25	0.008	0.03	0.02	0.20	0.03	0.037	< 0.02

Fig. 1—A schematic showing the tailor hot stamped 3-Point Bend and Axial hat-section rails. The white boxes indicate the locations where the sub-size dog-bone tensile specimens were extracted. Dimensions are in mm.

Table II. Tailored Hot Stamping Parameters Used to Develop the Tailored Material Conditions (TMCs) Examined in this Work

Tailored Material Condition	Part Type	Sheet Thickness (mm)	Die Temperature (°C)	Quench Time (s)	Avg. Vickers Hardness (HV$_{1000}$)
TMC1	axial	1.2	700	4	193
TMC2	3-point bend	1.2	600	10	222
TMC3	axial	1.2	400	4	290
TMC4	3-point bend	1.8	400	10	319
TMC5	3-point bend	1.2	400	10	376
MART	axial	1.2	25	4	486

quench time, and sheet metal thickness as shown in Table II. Quench time refers to the time between which the die is fully closed and opened again. Also shown in Table II is the measured average Vickers hardness for each material condition and shows that the softest tailored material condition occurs at the highest die temperature (TMC1) and the hardest material condition occurs at the lowest die temperature (MART).

C. Effect of Die Temperature on the Predicted Temperature-Time History

It is nearly impossible to physically measure the temperature-time history at a point within a part that has undergone the hot stamping process, therefore researchers typically rely on advanced finite element (FE) models to simulate the process and retrieve the temperature data. Using an explicit dynamic FE code (LS-Dyna), coupled thermal-mechanical-microstructural finite element models were developed by Omer *et al.*[19] to simulate the hot stamping process (blank transfer, forming, quench, and air cooling) for TMC1, TMC3, and MART. They predicted the temperature-time histories for these three material conditions as shown in Figure 2 and are presented here to give context on how some of the tailored microstructures, that will be analyzed in this work, were formed. The temperature-time history was extracted from an element within the FE model that is approximately located as shown in Figure 1, where plastic deformation was negligible. Overlaid in Figure 2 is the continuous
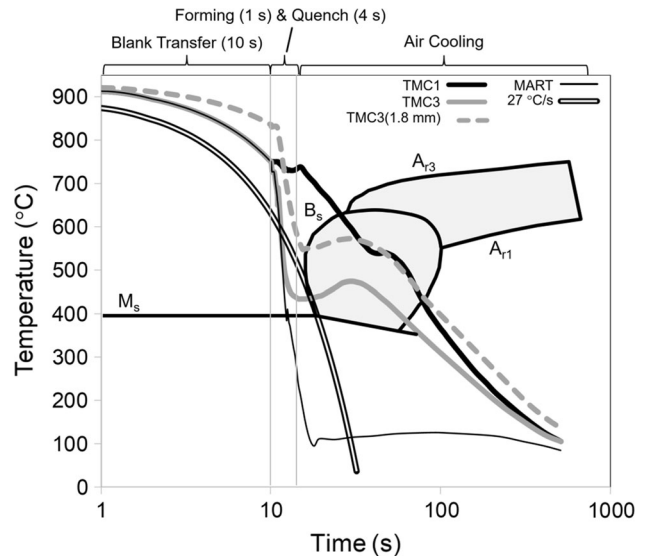

Fig. 2—The predicted temperature-time curves for the TMC1, TMC3, and MART material conditions. The CCT diagram for Usibor® 1500-AS is overlaid for reference only. The CCT diagram is adapted from Ref. [20].

cooling transformation (CCT) diagram, along with the critical cooling rate of 27 °C/s curve for the Usibor® 1500-AS boron steel used in this work. The authors recognize that the cooling rates imposed to generate TMC1 and TMC3 are highly non-linear, hence the CCT is included for discussion purposes only.
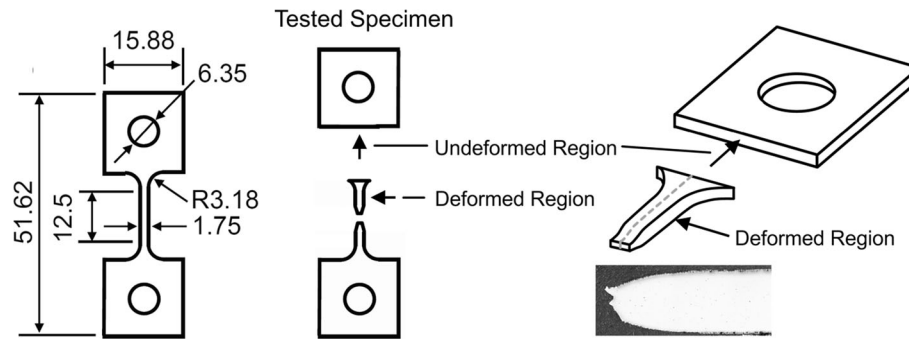
Fig. 3—Sub-size dog-bone specimen geometry (dimensions are in mm) and the locations of the tested specimens used for metallographic analysis. The arrows indicate the direction of the view for the undeformed (microstructural characterization) and deformed (damage characterization) regions of the tested specimens. Observations were made through-the-thickness of the specimen.

The 10 second blank transfer simulation predicts the temperature reduction due to convective cooling from 930 °C (the experimental austenitizing temperature). The second simulation is the forming operation (1 second) in which the die travels from fully opened to fully closed. The third simulation is of the quench process, where the die is fully closed for 4 seconds. The final model simulated the air-cooling operation, after the part is released from the die and allowed to convectively cool to ambient conditions. For the MART condition, the expected fully martensitic solid-state phase transformation was predicted due to the high quench rate imposed by a 25 °C die temperature. For TMC1 and TMC3, the cooling rate during quenching was reduced (compared to MART) and the temperature at the end of the 4-seconds quench period was higher than the prescribed die temperature (Table II) because of the increase in die temperature due to heat transfer from the blank. Upon release from the die, the predicted temperature of TMC3 remained approximately constant and then increased due to the latent heat of transformation when bainite began to transform. The TMC3 model did not predict the transformation of martensite or ferrite. The predicted temperature-time of the TMC1 model during air cooling resulted in a temperature increase shortly after the 4-seconds quench, which was due to the solid-state transformation of austenite into ferrite. The completion of the solid-state transformation was then shown to occur at approximately 550 °C. Due to the non-linearity of the TMC1 cooling rate, and the austenite to ferrite activation energy values used in the models, the start and completion of the phase transformation do not align with A_{r3} and A_{r1} of the CCT diagram, but predict the transformation of ferrite, as will be shown in the proceeding section.

The difference between TMC4 and TMC5 is the blank thickness, which was 1.8 and 1.2 mm, respectively. These two conditions were not modeled, but the effect of blank thickness was shown in Reference 19 for TMC3. The temperature-time history of a 1.8-mm blank, which had undergone the same hot stamping process as TMC3, was predicted and is shown as TMC3(1.8 mm) in Figure 2. The temperature at the start of the forming operation is greater for the thicker sheet due to the increase in thermal mass and reduction in heat loss during the transfer operation. The increase in sheet thickness reduces the cooling rate during the quenching operation and prevents the blank from reaching the die temperature of 400 °C. This results in a higher temperature at the start of air cooling for a thicker part, which may result in the transformation of more bainite and less martensite when compared to the thinner sheet.

D. Uniaxial Tension Tests

Uniaxial tension tests were conducted on specimens machined from the 3-Point Bend and axial hat-section rails (Figure 1). The sub-size dog-bone style specimen (Figure 3) used in this work was developed by Smerd et al.[21] They demonstrated (along with Bardelcik et al.[7]) that the stress-strain curves from quasi-static tension tests conducted on ASTM (E 8M-04) specimens matched those of the sub-size specimens up to the ultimate tensile strength (UTS) but resulted in higher post-uniform elongation due to the ratio of the neck to gauge length of the two specimens. The total elongation measured from the sub-size specimens can be used to rank relative ductility.

An electro-mechanical tensile testing machine with a 10-kN load cell was used to conduct the quasi-static tests at a nominal strain rate of 0.003 s^{-1}. Specimen elongation was measured using a clip-on extensometer and the number of repeat tests (reported in Table III) conducted for each tailored condition varied from two to five, depending on specimen availability.

E. Area Reduction Measurements

After the tensile tests were completed, the cross-sectional area of every tested specimen (average of both halves) was measured using extended depth of field images captured with a Keyence VHX-5000 digital microscope as shown in Figures 4(a) and (b). These images were used to quantify the percent area reduction of the cross-section at fracture. Percent area reduction measurements are typically conducted on fractured standard (such as ASTM) uniaxial dog-bone specimens, not the miniature dog-bone specimens that are the focus

Table III. Uniaxial Tensile Test Results for All of the Tailored Material Conditions

Tailored Material Condition	Number of Repeat Tests	Avg. Vickers Hardness, (HV$_{1000}$)	Avg. Yield Stress (MPa)	Avg. Ultimate Tensile Strength (MPa)	Avg. Uniform Elongation, Eng. (mm/mm)	Avg. Total Elongation, Eng. (mm/mm)	Pct Area Reduction
TMC1	5	193	383 [372/395]	615 [610/620]	0.14 [0.13/0.14]	0.24 [0.23/0.25]	79
TMC2	3	222	462 [460/464]	718 [710/724]	0.11 [0.11/0.13]	0.22 [0.21/0.24]	71
TMC3	2	290	664 [663/664]	842 [841/844]	0.05 [0.05/0.05]	0.11 [0.11/0.12]	73
TMC4	3	319	753 [742/774]	939 [931/954]	0.05 [0.05/0.05]	0.13 [0.13/0.13]	77
TMC5	3	376	869 [861/876]	1122 [1101/1136]	0.05 [0.04/0.05]	0.11 [0.11/0.11]	68
MART	3	486	1184 [1171/1204]	1556 [1550/1559]	0.05 [0.04/0.05]	0.10 [0.10/0.11]	60

The data in the square brackets represent the maximum and minimum measurements made from the population of repeat tests.
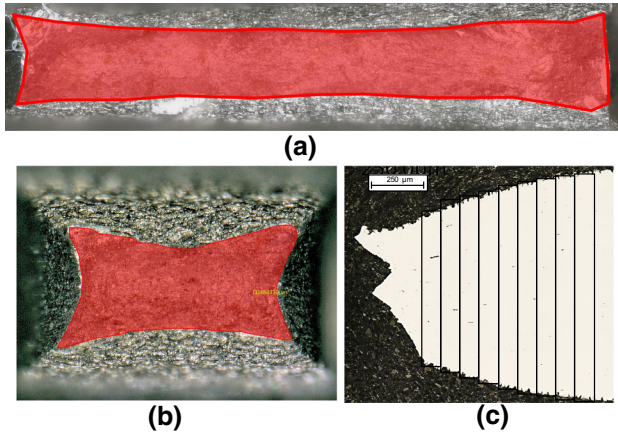

Fig. 4—An extended depth of field optical image of a fracture surface for (*a*) an ASTM E8 sub-size dog-bone specimen and (*b*) a miniature dog-bone specimen from the current work. (*c*) Areas within an as-polished specimen that were used to quantify the area fraction of voids and TiN particles.

of this work. A small study was conducted to investigate the effect of dog-bone specimen geometry (miniature *vs* ASTM E8 sub-size) for a number of 22MnB5 tailor hot stamped microstructures that were presented in Reference 7. The results of the percent area reduction measurements are shown in Figure 5(d) (with linear trendline fit) and indicate an approximate 10 pct area reduction offset between the two dog-bone geometries, with the miniature dog-bone specimens exhibiting a greater area reduction than the ASTM specimens. Figures 4(a) and (b) show example images of the area reductions for an ASTM E8 sub-size and miniature dog-bone specimen, respectively. Based on qualitative observations of the fracture surface geometries in Figure 4, the triaxiality (or stress-state) of the larger ASTM specimen is approximately that of plane-strain, while the triaxiality of the miniature dog-bone specimen appears to be elevated. Also shown in Figure 5(d), is that the area reductions measured for the miniature dog-bone data from Reference 7 aligns with the miniature dog-bone area reduction data from the current work. Therefore, when discussing the changes in area reduction with respect to tailored material conditions in the present work, the reader should consider these

values to be approximately 10 pct greater than those measured from ASTM E8 dog-bone specimens.

F. *Micro-hardness*

A micro-hardness tester (with 1000 g load) was used to measure the Vickers hardness in this work. The micro-hardness measurements were conducted on the mounted and polished specimens (undeformed region in Figure 3) that were used for metallographic observations. A total of five measurements were made through-the-thickness of the sheet to establish the average hardness for each tailored material condition.

G. *Metallography*

From the repeat tensile tests, a single representative specimen (tested) was selected for metallographic examination. The authors recognize that a single specimen introduces uncertainty in the data and may not be representative of the sample population, but it will be shown (in Section III) that the excellent repeatability of the tensile test results supports the use of measurements from a single tested specimen. For a single tested specimen, two mounted specimens (pucks) were prepared.

One of the mounted specimens was from the undeformed region, which was used to characterize and quantify the microstructure. All of the observations made on the undeformed specimen were at the center of the section as indicated by the arrow in Figure 3. In References 18, 19 hardness measurements were made along the gauge length of the sub-size dog-bone specimens used in the current work. The measurements revealed a constant hardness along the gauge length, indicating a consistent microstructure throughout.

The second mounted specimen was from the deformed gauge length as indicated by the section highlighted with the dashed line in Figure 3. The deformed gauge length specimens were used to quantify damage accumulation.

All of the mounted specimens were plane ground and polished using 500, 1200, and 4000 grit SiC paper, which was followed by 3- and 1-μm diamond paste. A non-drying colloidal silica suspension was used for the final polishing step. Ultrasonic cleaning was done between every polishing step.
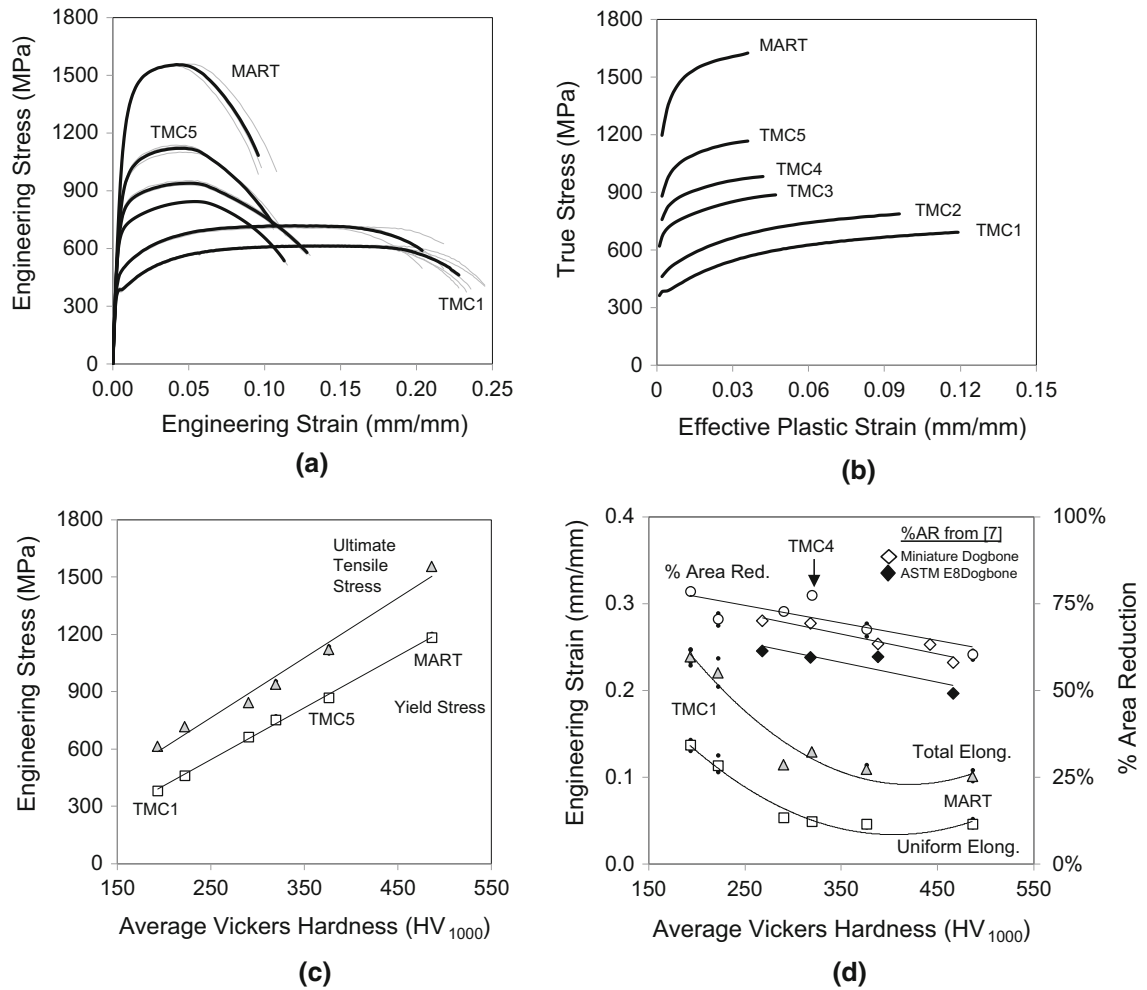
Fig. 5—The average (*a*) engineering stress-strain and (*b*) true stress *vs* effective plastic strain curves for TMC1 to MART. The average (*c*) strength and (*d*) elongation/area reduction data plotted *vs* HV_{1000}. The Miniature Dog-bone percent AR data in (*d*) were extracted from Ref. [7]. The small black data points represent the individual repeat test data for each conditions, while the open data points represent the average values.

Table IV.   The Average Measured Percent Area Fraction of Phases Present in the Tailored Material Conditions

Tailored Material Condition	Pearlite	Ferrite	Bainite*	Martensite	Wt Pct Carbon of Martensite
TMC1	26	73	—	< 1	—
TMC2	20	72	—	8	0.6
TMC3	—	22	65	13	1.5
TMC4	—	< 1	80	19	1.0
TMC5	—	—	46	54	0.4
MART	—	—	—	100	0.2

*All variants of Bainite (B1 and B2) are quantified as a single phase.

The undeformed specimens were etched with a 5 pct nital solution for 8 seconds to reveal the microstructure. An FEI Quanta 250 field emission scanning electron microscope (FE-SEM) was used to generate three separate micrographs (top, middle, and bottom surface of the sheet) for each tailored material condition. For each micrograph, the phases were manually delineated (selected) and a pixel count was conducted to determine the area fraction of each phase. The results of the three micrographs were then averaged to establish the multi-phase area fractions for each tailored material condition as presented in Table IV.

The deformed specimens were first observed using a Keyence VHX-5000 digital optical microscope in the as-polished condition to quantify the void area fraction and void density. A tiled micrograph was created for a single specimen at a magnification of 3000 times near the localized (necked) region as shown in Figure 4(c). The

entire image was then dissected into separate areas along the length of the specimen as shown in Figure 4(c). Each area corresponded to a different true thickness strain, which was calculated (to produce positive strains) as,

$$\varepsilon_{\text{thickness}} = \ln \frac{t_{\text{initial}}}{t_{\text{current}}}, \qquad [1]$$

where t represents the initial and current average thickness for each section. After applying thresholding methods, a pixel count was conducted to quantify the void and TiN area fraction for each thickness strain. The minimum void size detected in this work was 4×4 pixels, which corresponds to 0.1 μm^2. An example of an optical image of a void with a TiN particle is shown in Figure 10. Upon completion of the optical microscopy work, the mounted specimens were etched with a 5 pct nital solution for 8 seconds to reveal the microstructure. The FEI Quanta 250 FE-SEM was then used to capture detailed images of voids. The chemical composition of inclusions associated with some voids was also characterized using an Oxford Instruments energy-dispersive X-ray spectroscopy (EDX) analysis unit within a Jeol JSM 6460 SEM.

III. EXPERIMENTAL RESULTS AND DISCUSSION

A. Uniaxial Tensile Tests

The tensile testing results for the tailored material conditions investigated in this work are presented in Table III and plotted in Figure 5. The area reduction measurements are shown in Figure 5(d).

For the five tailored material conditions (and MART condition) examined in this work, the average engineering stress-strain and true stress vs effective plastic strain (flow stress) curves are shown in Figures 5(a) and (b), respectively. These average curves were generated from the repeat tests conducted for each tailored material condition. In Figure 5(a), the repeat test data are shown as the thin gray curves. The average yield stress (0.2 pct offset method), average ultimate tensile strength, average uniform elongation, and average total elongation are presented in Table III and plotted in Figures 5(c) and (d), respectively. Included with the average values, are the minimum and maximum values from the population of repeat tests. Based on the excellent repeatability of the test results for each tailored condition, it was judged acceptable to assume that the phase composition for each of the repeat specimens was the same.

The tensile behavior of these tailored material conditions shows the expected linear increase in tensile stress and yield stress for increasing hardness levels as shown in Figure 5(c). The total elongation is greatest for TMC1 (0.24) and TMC2 (0.22), which were created using a heated die temperature of 700 °C and 600 °C, respectively. The good balance of strength and ductility makes these softer tailored material conditions excellent candidates for use in tailored crash structures. For TMC3 and greater, the tensile and yield stress

progressively increase with increasing hardness, but the total elongation is noticeably reduced and ranges from 0.10 to 0.13. This was also observed by Bardelcik et al.[7] and Eller et al.[14] for bainitic and mixed bainitic/martensitic tailored material conditions. The flow stress curves for TMC1 to TMC4 indicate a similar strain hardening response, with a scaling of the overall strength in the vertical axis as shown in Figure 5(b). The strain hardening rate increases for the strongest conditions TMC5 and MART.

B. Percent Area Reduction

Percent area reduction can be used to quantify a materials' fracture strain, often after the onset of necking and serves as another measure of metal ductility. A more ductile material can sustain a greater area reduction as shown by the highest percent area reduction for the TMC1 tailored material condition, which also exhibits the greatest total elongation. The general trend shown in Figure 5(d) indicates a decrease in percent area reduction for increasing hardness levels. The TMC4 tailored material condition area reduction appears as an outlier in the dataset because of the relatively high post-uniform elongation as shown in the engineering stress-strain curve for TMC4 in Figure 5(a). It should be noted that this tailored material condition was the only one with a sheet thickness of 1.8 mm. This post-uniform elongation behavior may have been affected by a different stress-state (triaxiality) for this thicker specimen.

C. Microstructural Analysis

The multi-phase microstructures of the five tailored material conditions were quantified using the micrographs shown in Figure 6 (excluding MART). The resolution of these high-quality micrographs clearly distinguished the various multi-phase constituents which were used to quantify the area fractions of the multiple phases. An example of the post-processed micrographs used to quantify the area fractions are shown for TMC1 to TMC5 in Figure 6. The average area fractions for the tailored material conditions examined in this work are presented in Table IV and plotted in Figure 7. Figure 7 shows the (low) measured standard deviation from the three separate micrographs used to quantify the area fractions for each tailored material condition. The general trend shown in Figure 7 indicates that the tailored microstructures transition from lower strength and more ductile phases (pearlite and ferrite) to higher strength and low ductility phases as the in-die heating temperature reduce from 700 °C (TMC1) to 25 °C (MART).

1. Carbon content of martensite

In the proceeding FE-SEM micrographs, it will be shown that the appearance of the martensitic phase varies with respect to the tailored material condition. This can be attributed to the carbon content of the martensite. Krauss[22] provides an extensive review of martensite and shows that a ~ 0.22 wt pct carbon
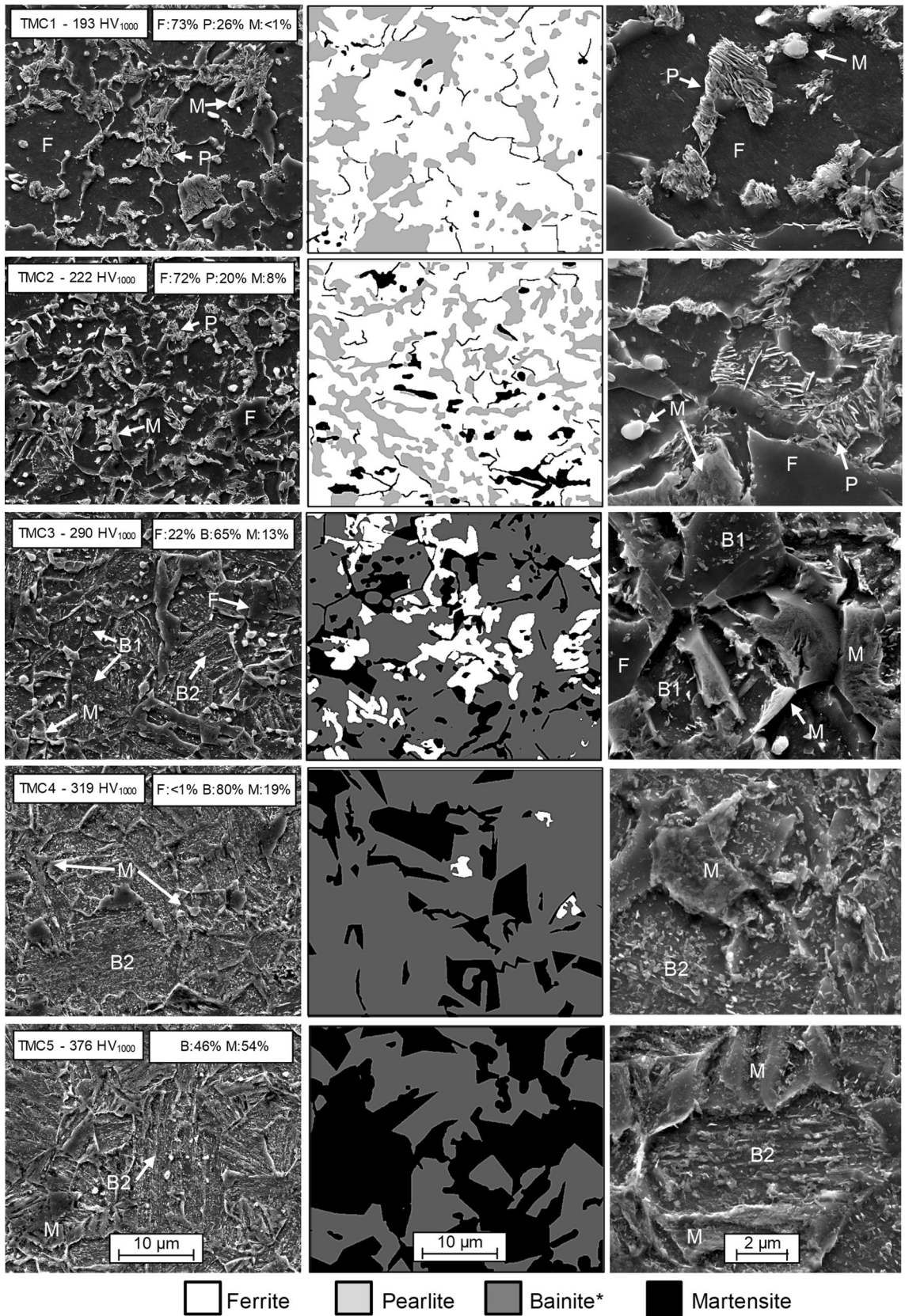
Fig. 6—Original and post-processed SEM micrographs of the five different tailored material conditions. All variants of Bainite (B1-B2) are quantified as a single phase.
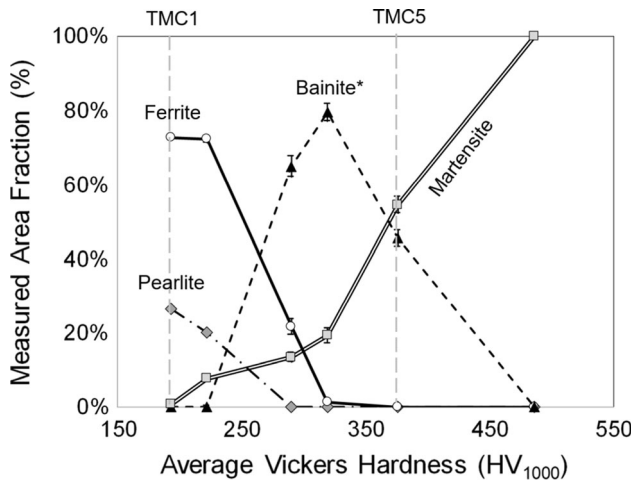
Fig. 7—The variation in measured area fraction of pearlite, ferrite, bainite, and martensite with respect to the average hardness of each tailored material condition. The error bars indicate ± the standard deviation as measured from the three repeat micrographs that were quantified for each material condition. All variants of Bainite (B1-B2) are quantified as a single phase.

martensite will exhibit a hardness of approximately 500 HV, which aligns with the MART material condition (486 HV_{1000}) examined in this work. It is also well established in the literature that martensite with a weight percent carbon of ~ 1.0, exhibits a hardness on the order of 900 HV.[22] In multi-phase steels, high carbon content martensite (which was observed in this work) is typically associated with some retained austenite, hence the use of the term M/A (martensite/austenite) to describe this type of martensite within the literature.[22–25] By conducting a simple mass balance, carbon partitioning during the transformation of austenite into daughter phases can be calculated as follows:

$$C_\gamma = \frac{\bar{C} - V_f C_f - V_b C_b - V_p C_p}{1 - V_f - V_b - V_p}, \qquad [2]$$

where C_y is the remaining wt pct carbon concentration in austenite, which can be taken as the wt pct carbon concentration in the as-quenched martensitic phase. $\bar{C}$ is the as-received wt pct carbon content of the bulk material, 0.22 in this case. V_f, V_b, and V_p represent the measured volume fractions of the ferrite, bainite, and pearlite, respectively, which are presented as average area fractions in Table IV for each material condition. A carbon content of 0.022 wt pct is assigned to the transformed ferrite phase (C_f) as suggested by Chen and Cheng[26] and the bainitic ferrite carbon content (C_b) in solid solution was taken as 0.03 wt pct as suggested by Bhadeshia and Edmonds.[27] Because bainite exists in various forms (i.e., upper, lower, granular, lath-like, etc.), the authors acknowledge that selecting a single C_b value is an approximate assumption, considering that the decomposed bainite phases vary with respect to tailored material condition as will be shown in the proceeding sections for the current work. Zhang and Kelly[28] provide a good review on the reported carbon content of bainite in the literature, which varies among researchers. The carbon content of

pearlite (C_p) was chosen as 0.8 wt pct and the calculated wt pct of carbon present in the martensite for each material condition is shown in Table IV. Because of the relatively small area fraction of martensite in TMC1, the calculated carbon wt pct of martensite is unreliable, but assumed to be high. For all of the other material conditions, the trend indicates an increase in the martensitic carbon concentration up to TMC3, then a reduction in concentration to the expected value for MART. Based on these results, the hardness/strength of the observed martensite (other than MART) will be high and may fall into the category of M/A.

2. TMC1 microstructure

This tailored material condition resulted in the lowest measured tensile strength and greatest total elongation at 615 MPa and 0.24, respectively. It is the only material condition which exhibited an upper yield point as shown in Figures 5(a) and (b). The micrograph for this tailored material condition is shown in Figure 6 and clearly indicates a ferritic and pearlitic microstructure, with area fractions of 73 and 26 pct, respectively. The excellent ductility of this material is a result of the high area fraction of ferrite and the relatively large grain size of this phase as shown in the post-processed micrographs in Figure 6. In addition to the two dominant phases, approximately 1 pct area fraction of a hard and featureless phase was observed. This hard phase is martensite (or M/A), or a carbide, and exists as small individual grains dispersed throughout the microstructure and typically located along grain boundaries. This type of martensite is similar to the M/A structure observed by Li and Baker.[24] The martensitic phase was also observed with a banded (or stringer) morphology throughout the thickness of the sheet, but only in small amounts. The ferritic phase shown in Figure 6 high magnification micrograph shows the presence of a finely dispersed constituent (which may be a carbide) present in some of the ferrite grains.

3. TMC2 microstructure

Similar to TMC1, this tailored microstructure also consisted of ferrite, pearlite, and martensite, with area fractions of 72, 20, and 8 pct, respectively. The tensile strength is 718 MPa (17 pct increase relative to TMC1) and the total elongation strain was reduced from 0.24 to 0.22 (8 pct decrease). Comparing the two microstructures, the increase in strength can be attributed to an overall refinement of the microstructure and an increase in the area fraction of the martensitic phase. Similar to TMC1, the presence of a finely dispersed constituent was observed in some of the ferrite grains.

4. TMC3 microstructure

When compared to TMC2, a further reduction in total elongation was observed for TMC3 to a value of 0.11 strain, with a tensile strength of 842 MPa. In fact, the total elongation of this tailored material condition is similar to that of MART, which has a tensile strength of 1556 MPa. The dominant microstructure in this case is bainite with an area fraction of 65 pct as shown in Figure 6. For the total measured area fraction of

bainite, two variants of the phase were observed, B1 and B2. The B1 phase consists of a ferritic matrix with randomly oriented carbides dispersed throughout the grain, which was also observed by Banjerjee.[29] In some cases, the B1 microstructure has such a low density of carbides present, that it may be considered ferrite. The second bainitic phase (B2) consists of a more aligned bainitic ferrite with a lath structure that can be characterized as a lath-like upper bainite[14,30–32] with finely dispersed carbides throughout the grains. Martensite islands are dispersed throughout the microstructure at an area fraction of 13 pct and ferrite is present at 22 pct as well. The martensite (or M/A) islands exist along grain boundaries and at grain boundary junctions. This martensite contains the highest calculated carbon content (see Table IV).

5. TMC4 microstructure

The dominant phase in this microstructure is bainite (B2 variant) at 80 pct area fraction. The bainite grain size is relatively large as shown in Figure 6. Martensite is present at 19 pct area fraction and the absence of ferrite and the B1 bainitic structure resulted in an increased tensile strength to 939 from 842 MPa (TMC3). The martensite grains are larger than those found in TMC3, with a high calculated carbon content. Less than 1 pct of ferrite was also observed for this material condition. The post-uniform stress-strain behavior for this material condition (Figure 5(a)) is slightly different when compared to TMC3 and TMC5. The difference can be attributed to the thickness of this tailored material condition, which was 1.8 mm, compared to 1.2 mm for all other conditions as shown in Table III. The width of the tensile specimens was constant for all tailored material conditions; therefore the triaxiality near the onset of fracture of the 1.8-mm TMC4 specimen was different, hence affecting the post-uniform stress-strain behavior. This will be verified in future numerical work.

6. TMC5 microstructure

This tailored material condition consists of a mixed martensitic (54 pct) and bainitic (46 pct) microstructure. Similar to TMC3 and TMC4, the lath-like bainitic (B2) structure was observed. The martensitic grains consist of the characteristic packets of lath crystals that are associated with lath martensite in steels containing less than 0.6 wt pct carbon.[22,33] The tensile strength is relatively high (1122 MPa) and due to the increased area fraction of martensite. The total elongation is similar to that of TMC3 and TMC4.

7. MART microstructure

This final material condition is fully martensitic, with some auto-tempered martensite (AM) that developed during the quenching process. The martensitic transformation start (M_s) and finish (M_f) temperatures are ~ 400 °C and ~ 250 °C, respectively.[20] Tempering occurs when the first martensite to form (just below M_s) is subject to high temperatures as the part is quenched. Jarvinen et al.[34] also observed AM in their extensive study on the final properties of various hot

stamped 22MnB5 steels. As expected, the strength of this martensitic material condition is 1556 MPa with a total elongation of 0.10 strain.

D. Damage Characterization

In this section of the work, the damage mechanisms and damage accumulation are characterized for each of the tailored material conditions. Also, the role of inclusions (titanium nitride and other non-metallics) is discussed.

1. Inclusions

For all of the tailored material conditions examined in this work, a detailed survey of the etched SEM micrographs was conducted to examine the influence of inclusions on damage. EDX chemical analysis was conducted to quantify the elemental composition of the material adjacent to voids that were associated with suspected inclusions. Some of the analysis areas (numbered boxes) are shown in Figure 8 with the results of the corresponding chemical analysis presented in Table V. Qualitatively, the dominant inclusion observed for all of the tailored material conditions was titanium nitride (TiN) as shown in Figures 8(a), (c), and (e). The influence of TiN particles on damage is discussed in the proceeding section. Non-metallic oxide inclusions were also observed at some voids as shown in Figures 8(d), (e), and (f). The number of voids associated with the observed non-metallic oxide inclusions was not quantified in this work, but from a qualitative perspective, the presence of these inclusions was very low and it is assumed that they had little influence on damage accumulation within these tailored material conditions. Although the influence of the observed non-metallic oxide inclusions on damage appears to be minimal, the effect of aluminum-oxide inclusions has been shown to affect the fatigue behavior of hot stampings and needs to be considered.[35]

2. Titanium nitride particles

For all of the tailored material conditions examined in this work, titanium nitride (TiN) particles were observed throughout the microstructure as confirmed via EDX chemical analysis (see Figure 8 and Table V). Titanium is typically added to prevent austenite grain coarsening and used to consume nitrogen during the steelmaking process.[36,37] The variation in titanium nitride (TiN) particle shape observed in this work is shown in Figure 9. The majority of the particles observed had a uniform (square) shape with an aspect ratio near unity. On average, a large square particle was ~6 x 6 μm, with the largest observed particle for all of the conditions being 7 × 9 μm. Elongated particles were also common with aspect ratios up to ~ 3. A small number of irregularly shaped particles were also observed. The area fraction of TiN particles was quantified during the void area fraction quantification using optical micrographs of the fractured specimens in the as-polished state. The distinct color of these particles (see Figure 10) was used to quantify an average TiN area fraction of
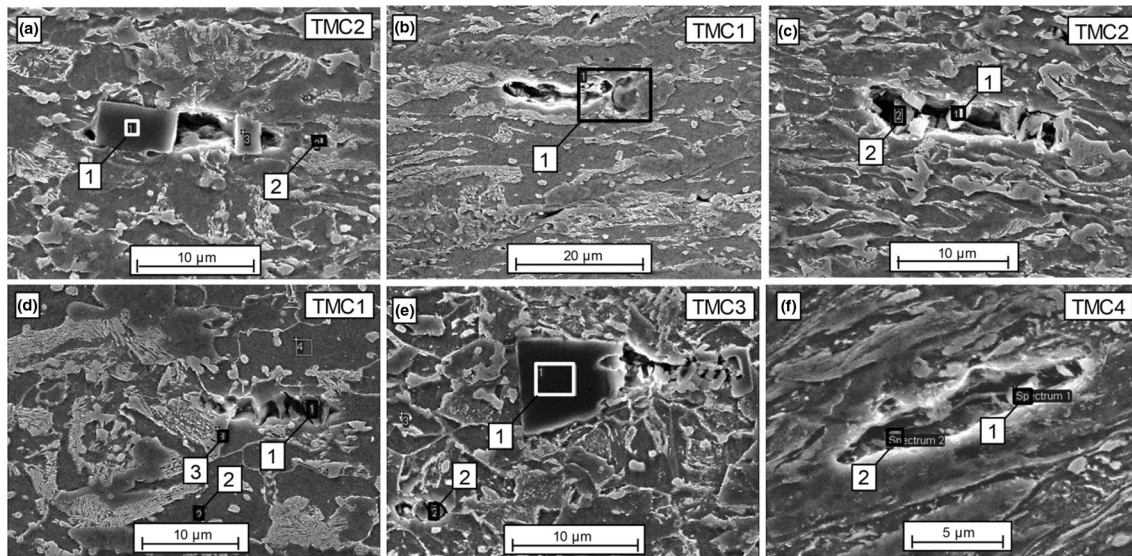
Fig. 8—SEM micrographs of voids associated with inclusions for various tailored material conditions. The highlighted areas represent the scan window for the EDX chemical analysis that is presented in Table V. The areas shown above indicate the particle types for varying tailored material conditions: (*a*) TMC 2-TiN particles, (*b*) TMC1-iron-rich particle, (*c*) TMC2-TiN particles, (*d*) TMC1: non-metallic inclusion and iron-rich particles, (*e*) TiN particle and non-metallic inclusion, and (*f*) non-metallic inclusions.

Table V. EDX Results of the Chemical Analysis Conducted on the Areas Shown in Fig. 8

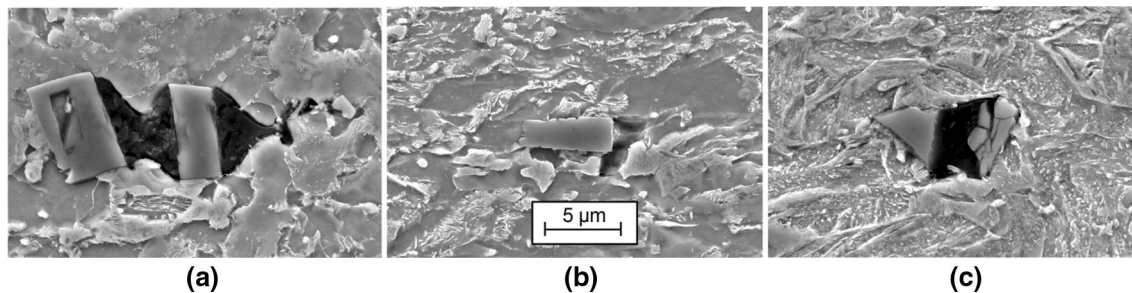| Figure 10 Scan Area	N	O	Mg	Al	Ca	Ti	Cr	Mn	Fe
a-1	5.2	—	—	—	—	94.8	—	—	—
a-2	—	—	—	—	—	33.1	—	—	66.9
b-1	—	—	—	—	—	—	—	2.4	97.6
c-1	7.8	—	—	—	—	92.2	—	—	—
c-2	9.0	—	—	—	—	91.0	—	—	—
d-1	—	21.1	27.4	12.7	8.4	—	—	—	30.4
d-2	—	—	—	—	—	—	—	1.9	98.1
d-3	—	—	—	—	—	—	—	2.4	97.6
e-1	15.1	—	—	—	—	82.6	—	—	2.3
e-2	—	16.7	—	17.4	14.6	—	—	—	51.3
f-1	—	20.1	10.9	10.5	8.3	2.8	—	—	47.4
f-2	—	14.2	—	10.9	7.0	6.2	—	—	61.7

Results are in atomic percent.

Fig. 9—Variation in TiN particle shape: (*a*) square, (*b*) elongated, and (*c*) irregular shape. The scale marker is common for all three micrographs.

~ 0.04 pct for all of the tailored material conditions examined in this work.

Recent studies[38,39] on the damage behavior of complex phase steels with tensile strengths of ~ 800 MPa have shown that TiN particles (within the size range of those examined in this work) strongly affect void nucleation, growth, and coalescence within these advanced high-strength steels. Both studies showed that void nucleation occurred due to particle cracking and decohesion of the particles with the surrounding matrix.

Using microtomography, Scott et al.[38] concluded that large TiN particles with cubic geometries were associated with larger voids and culminated in a single, large coalescence event at high plastic strains. They also found that small and irregularly shaped TiN particles resulted in smaller coalescence events.

3. Void accumulation

The percent void area fraction was quantified with respect to true thickness strain in Figure 11. The total void area fraction is shown as the black data points and includes all of the measured voids associated with and without TiN particles. The total void area fraction data included some extremely large voids (up to ~ 5 × 10 μm) which were associated with TiN particles. Since these particles are randomly distributed, some of the thickness area regions (rectangles in Figure 4(c)) contain more TiN particles than others. This sometimes causes the variation in total void area fraction to be large from one thickness strain measurement to the next. This is highlighted for the three highest thickness strains measurements in Figure 11(b). The large voids associated with TiN particles were easily identified in the optical images (see Figure 10), therefore a second void accumulation dataset is plotted (gray data points) in which the voids due to the TiN particles, were subtracted from the total measured void area fraction. This resulted in a void accumulation response due to the multi-phase interactions, not the TiN particles. As expected, this data shows less variation than the total void area fraction data for all of the tailored material conditions. Figure 11 shows the void density, or number of voids (voids greater than 4 pixels in area) per area (mm^2). The void density curves quantify the void nucleation rate for a particular tailored material
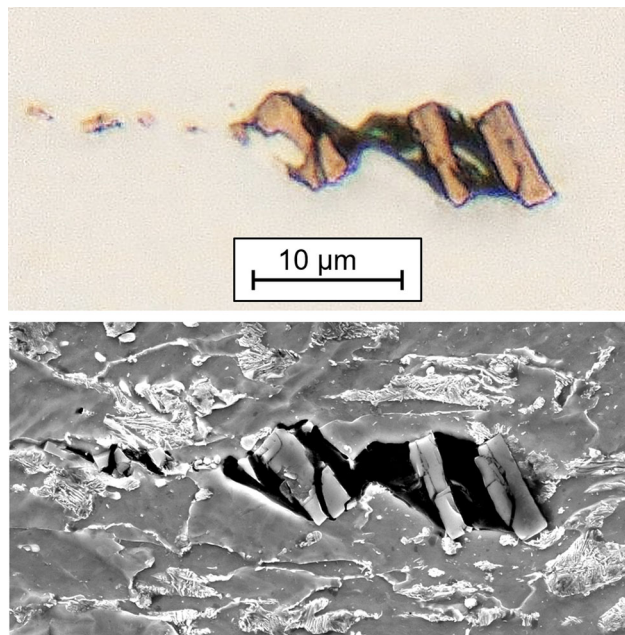

Fig. 10—An optical (used to quantify voids area fraction) and FE-SEM micrograph showing the distinct TiN particles.
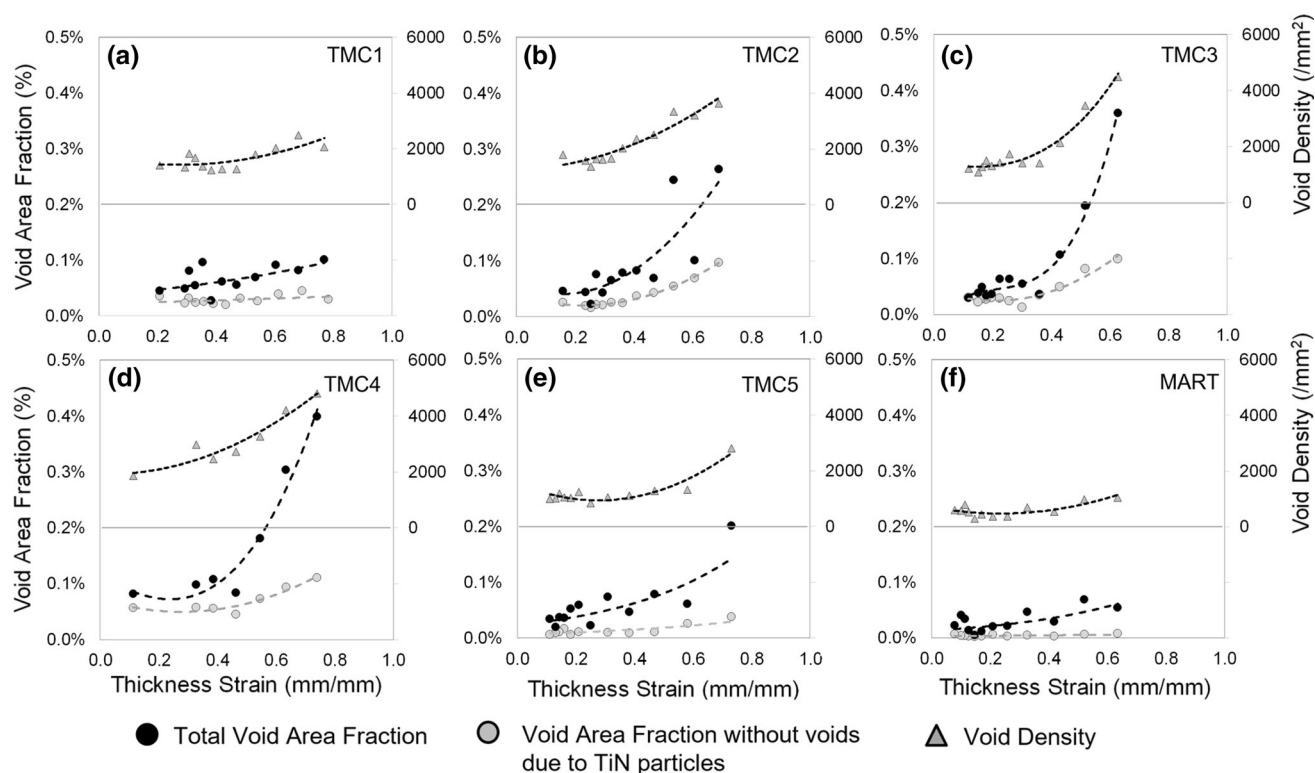

Fig. 11—The measured void area fraction and void density vs the true thickness strain for (a) TMC1, (b) TMC2, (c) TMC3, (d) TMC4, (e) TMC5, and (f) MART.
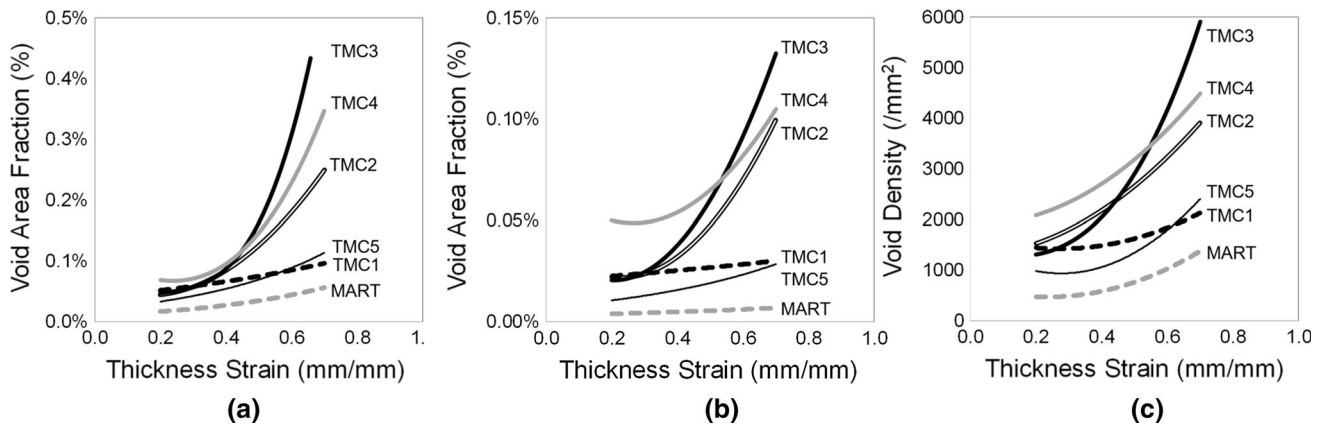
Fig. 12—The trend lines from Fig. 11, comparing the (*a*) total void area fractions, (*b*) void area fractions without voids associated with TiN particles, and (*c*) total void density *vs* thickness strain.
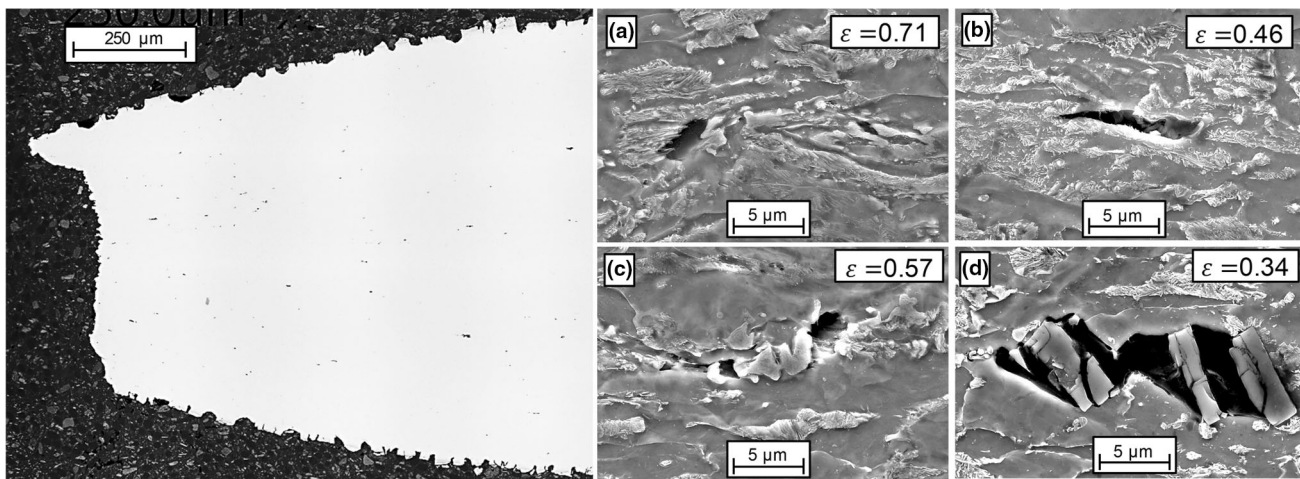

Fig. 13—SEM images of voids for TMC1 at true thickness strains of (*a*) 0.71, (*b*) 0.46, (*c*) 0.57, and (*d*) 0.34. The tensile direction runs horizontal to all images.

condition. For all three datasets presented in Figure 11, a trend line (polynomial) was fit to the data. The trend lines are plotted for all tailored material conditions in Figure 12.

4. *TMC1 and TMC2 damage characterization*

One may assume that the predominantly ferritic/pearlitic microstructures of these two tailored material conditions would result in similar rates of damage accumulation; however, the effect of increased martensite content and the refined grain size of TMC2, results in a higher rate of void accumulation as shown in Figures 11 and 12a and b. When subtracting the effect of the TiN particles, the measured void area fraction at ~0.60 thickness strain is 0.03 and 0.07 pct for TMC1 and TMC2, respectively (Figure 12b).

For both TMC1 and TMC2, void nucleation is shown to occur at the pearlite/martensite interface (Figure 13(a)), the pearlite/ferrite interface (Figure 13(b)), the martensite/ferrite interface (Figures 13(c), 14(a)), and at interfaces between each of the phases and the TiN particles

(Figures 13(d), 14(d)). Additionally, void nucleation was observed at some ferrite-ferrite grain boundaries, which appeared to be carbon enriched with a hard phase as shown in Figure 14(b). Similar grain boundary void nucleation observations have been made for microalloyed[24] and dual-phase (DP) steels.[40]

The majority of the observed void nucleation modes observed for these two tailored material conditions were associated with the hard martensitic phase and show similar mechanisms as those observed in commercial DP steels.[40–45] The main similarities between the current tailored materials and DP steels are that nucleation is shown to occur (1) between two separate martensite particles (Figure 13(a)) (2) between a cracked martensite particle (Figure 13(c)) and (3) due to decohesion of the softer phase and the martensite islands (Figures 13(a), 14(a)).

The higher martensitic content and refined grain structure of TMC2 (when compared to TMC1) results in an increase in void nucleation sites as demonstrated by the higher measured void density of TMC2
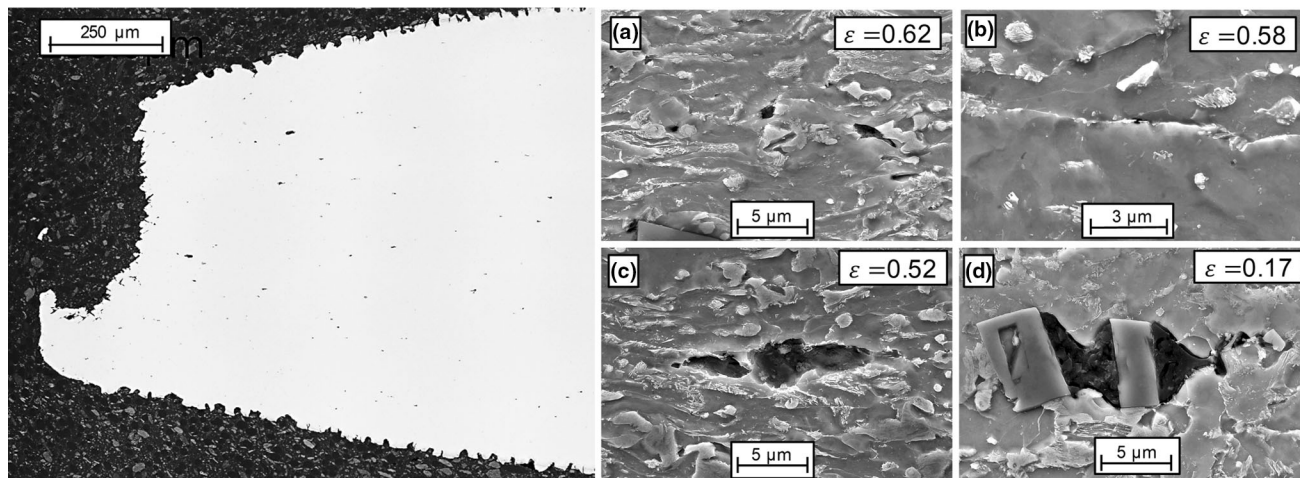
Fig. 14—SEM images of voids for TMC2 at true thickness strains of (*a*) 0.62, (*b*) 0.58, (*c*) 0.52, and (*d*) 0.17. The tensile direction runs horizontal to all images.
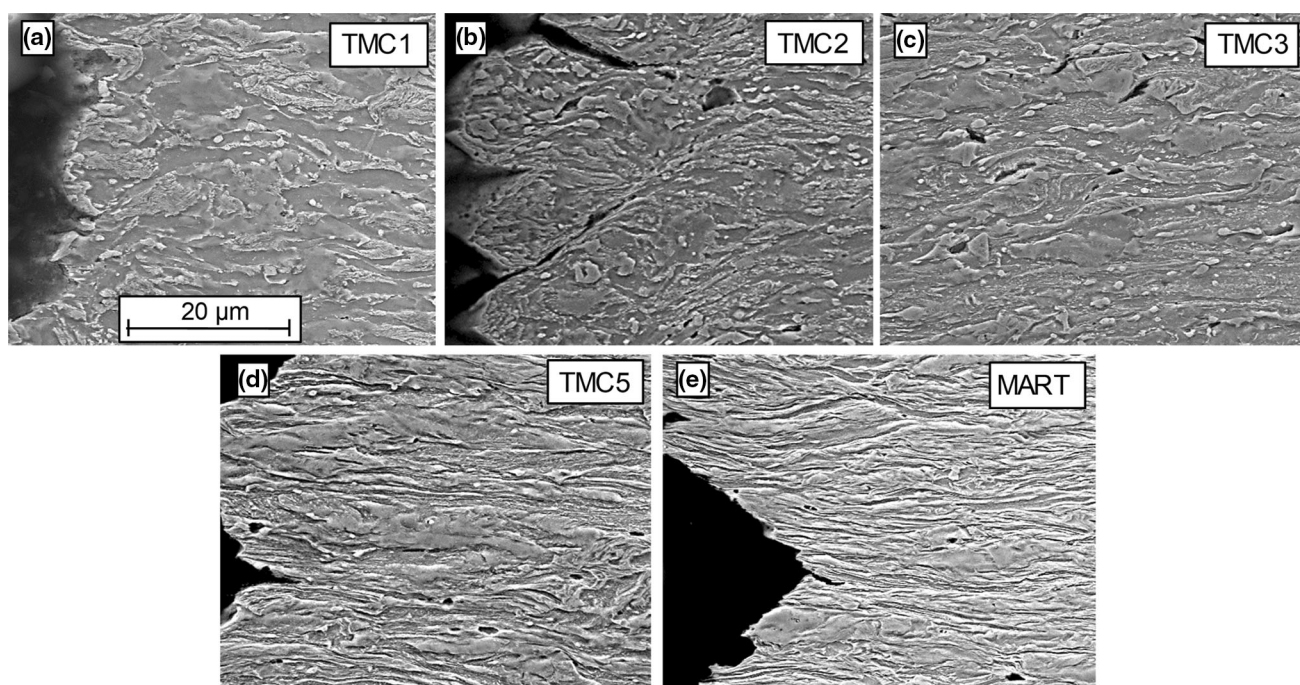

Fig. 15—Micrographs near the fracture surface of (*a*) TMC1, (*b*) TMC2, (*c*) TMC3, (*d*) TMC5, and (*e*) MART. The tensile direction runs horizontally.

(Figure 12(c)). Therefore, it can be assumed that the higher rate of void accumulation in TMC2 is nucleation driven, rather than growth (and/or coalescence) driven. This finding is also supported by the drop in the percent area reduction for TMC2, when compared to TMC1 in Figure 5(d). In Figure 15, TMC2 appears to have a greater level of damage (more voids near fracture surface and just inside) than TMC1 and void coalescence appears to occur along shear bands in TMC2, not TMC1. Away from the fracture surface, void growth is in the tensile direction for these two tailored material conditions. It should also be noted that even with the low martensitic area fraction in TMC1, the observed banded martensite structure was shown to facilitate void

nucleation and growth along the length of the bands as shown in Figure 16. This is a similar observation that was made by Lai *et al.*[40] for a commercial DP steel with a banded martensitic grain morphology. The banded structure resulted in martensite cracking, which led to the development of large voids between martensite particles.

Due to the high plastic deformation accommodated by the ferrite, the TiN particles observed in these two material conditions were found to be cracked and separated along the tensile axis as shown in Figures 13(d) and 14(d). These broken and separated TiN particles increase the void area associated with them and this phenomenon is likely due to a "void

propping" mechanism associated with the hard particles, as described by Thomson et al.[46]

5. TMC3 damage characterization

In this multi-phase microstructure, the number of potential void nucleation sites is high due to the finely dispersed martensitic islands near bainite/ferrite grain boundaries and grain boundary junctions. Qualitatively, this observation is shown in Figures 15(c) and 17(a). Even at low strains, voids have already nucleated and grown at these problematic grain boundary junctions as shown in Figure 17(d). This tailored material condition resulted in a (non-TiN) measured void area fraction of 0.09 pct at ~ 0.60 thickness strain (Figure 11(d)). When compared to the other tailored material conditions, the total (Figure 12(a)) and non-TiN (Figure 12(b)) void accumulation curves for TMC3 indicate the poorest damage resistance.

Void nucleation occurs predominantly at the interface between martensite and bainite/ferrite, with growth in the tensile direction (Figures 17(a) and (d)). The martensitic islands (in close proximity to one another) also tend to separate to nucleate voids (Figure 17(a)).
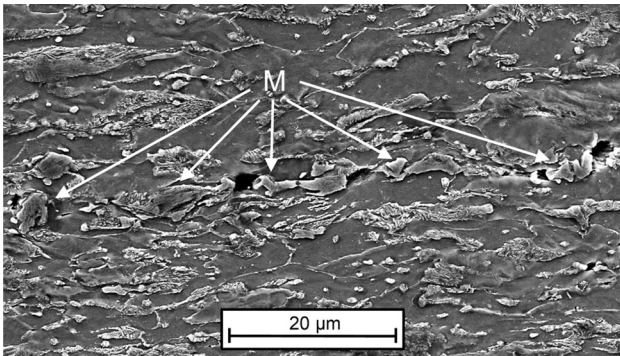

Fig. 16—Voids nucleated and grown along a martensite band found in TMC1. The tensile direction runs horizontal to the micrograph and thickness strain is ~0.60.

Martensite particle cracking appears to play a small role in void nucleation because of the finely dispersed martensitic islands, high strength of this martensite (high carbon content, Table IV), and its relatively low area fraction. The combined effect of these nucleation modes resulted in the highest measured void density (Figure 12(c)), indicating that void accumulation is nucleation driven. This observation aligns with the findings of Lai et al.[40] for DP steels, where the matrix is ferrite rather than a bainite/ferrite matrix as reported for TMC3 (13 pct martensite). They showed that the dominant void nucleation mode was decohesion for a low martensite volume fraction (15 pct) DP steel. As they increased the volume fraction on martensite, the void nucleation mode transitioned to martensite particle fracture. Erdogan[47] made similar observations regarding martensite grain morphology in DP steel, where finely distributed martensitic grains reduced the martensite cracking, nucleated via decohesion, and decreased the microvoid size. It should be noted that EDX analysis did not detect non-metallic elements in Figures 17(c) and (d).

When comparing TMC3 to TMC2, the difference in the total void area fraction curves (Figure 12(a)) is greater between these two tailored material conditions, than it is for the non-TiN (Figure 12(b)) void area fraction curves, which suggests that TiN particles have a stronger contribution to damage accumulation for this tailored material condition. The TiN particles were observed to nucleate voids at the interface between bainite/TiN (with subsequent growth, Figure 17(b)) and due to TiN particle cracking.

6. TMC4 and TMC5 damage characterization

These 2-phase tailored material conditions are similar in the sense that they are bainitic (B2 variant) with martensitic area fractions of 19 and 54 pct for TMC4 and TMC5, respectively. The increased martensite content of TMC5 results in a higher strength and only a slight decrease in total elongation when compared to
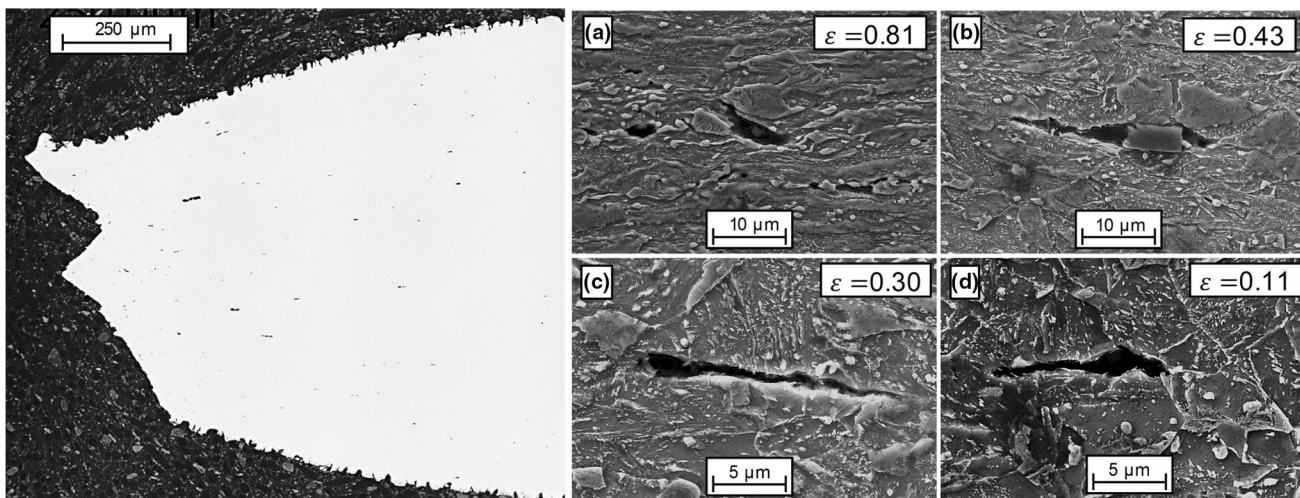

Fig. 17—SEM images of voids for TMC3 at true thickness strains of (a) 0.81, (b) 0.43, (c) 0.30, and (d) 0.11. The tensile direction runs horizontal to all images.
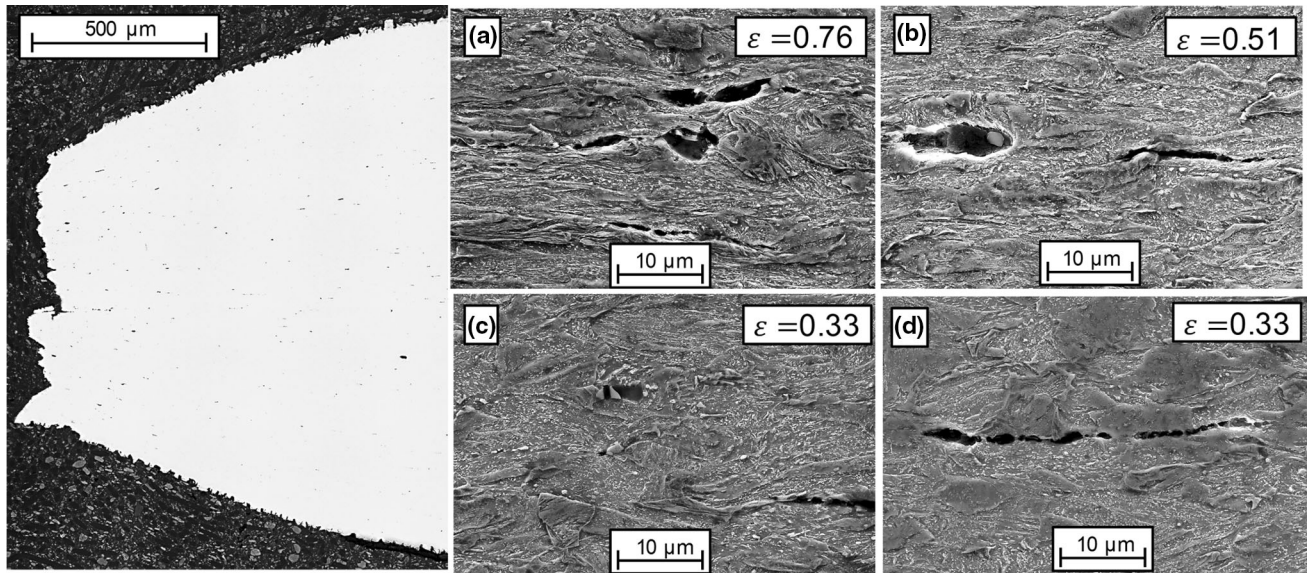
Fig. 18—SEM images of voids for TMC4 at true thickness strains of (*a*) 0.76, (*b*) 0.51, (*c*) 0.33, and (*d*) 0.33. The tensile direction runs horizontal to all images.
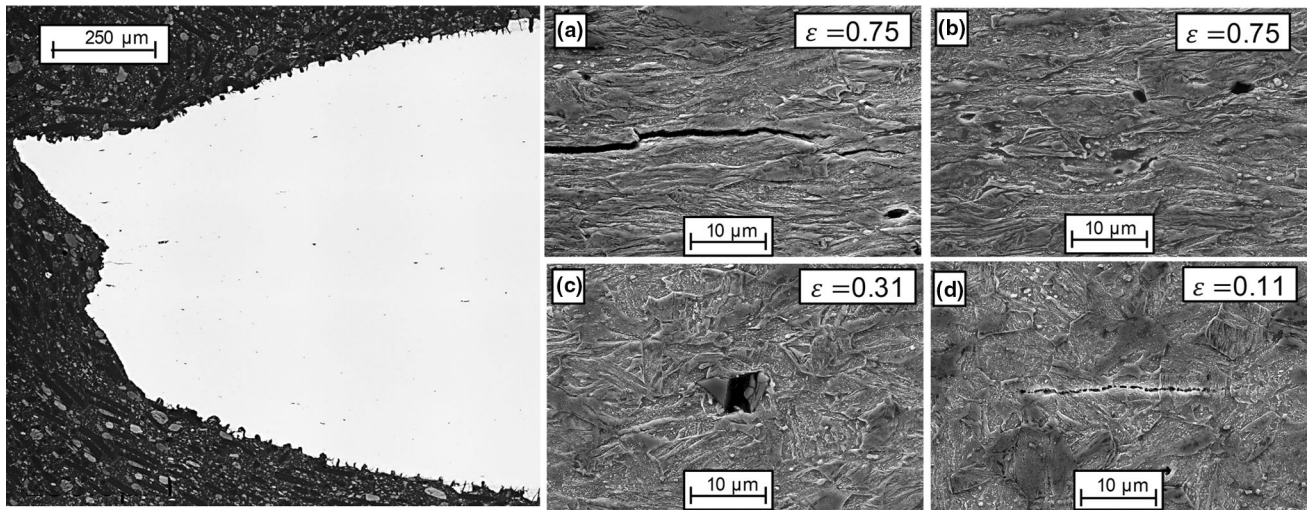

Fig. 19—SEM images of voids for TMC5 at true thickness strains of (*a*) 0.75, (*b*) 0.75, (*c*) 0.31, and (*d*) 0.11. The tensile direction runs horizontal to all images.

TMC4 as shown in Figure 5(a). The measured void area fraction (without TiN) at ~ 0.60 thickness strain is 0.08 and 0.03 pct for TMC4 and TMC5, respectively. When comparing the total (Figure 12(a)) and non-TiN (Figure 12(b)) void accumulation curves of these two tailored material conditions, it is quite evident that the microstructural makeup of TMC5 supresses damage more than TMC4.

Void density (Figure 12(c)) is also noticeably less for TMC5 and suggests that void nucleation is suppressed due to increased martensite content. The post-processed micrograph in Figure 6 shows that TMC4 consists of more finely dispersed martensitic grains (than TMC5) throughout the microstructure, which in some cases have formed at grain boundaries and grain boundary junctions. This leads to an increased number of potential

void nucleation sites. The void density at 0.2 thickness strain (Figure 12(c)) shows that void nucleation at low strains is the highest for TMC4, when compared to the other tailored material conditions. This suggests that voids nucleate easily and at low strains for this particular microstructure. The calculated carbon content of the martensite (Table IV) in TMC4 and TMC5 is 1.0 and 0.4 wt pct, respectively. Therefore, the higher strength martensite in TMC4 is more susceptible to void nucleation through martensite cracking, separation, and decohesion. A similar phenomenon was observed by Azuma *et al.*[48] for DP steel, in which the hardness of the martensite was varied by tempering. They concluded that a reduced hardness differential between the ferrite and martensite retarded void formation in the martensite due to an improvement in critical
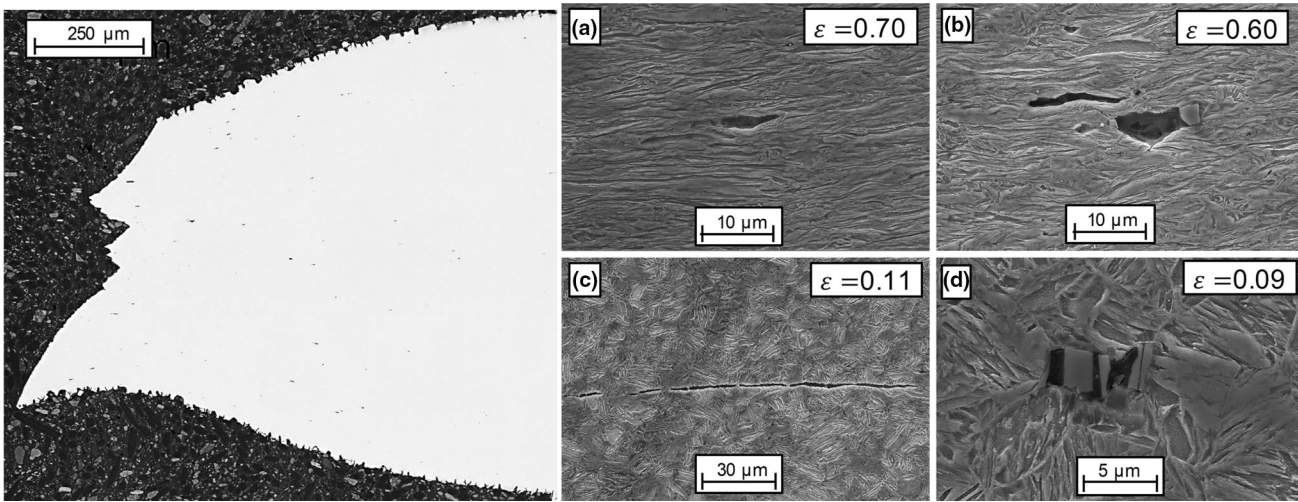
Fig. 20—SEM images of voids for MART at true thickness strains of (*a*) 0.70, (*b*) 0.60, (*c*) 0.11, and (*d*) 0.09. The tensile direction runs horizontal to all images.

strain for void formation. Also, as the volume fraction of martensite increases (for increasing TMC), the martensite grains become more coarse and exhibit similarities to the work of Kim and Thomas,[49] who heat-treated DP steels to vary the martensite morphology. They showed that a more coarse DP structure resulted in fracture within the ferrite matrix, while a more refined DP structure resulted in failure due to void nucleation and coalescence. This observation was also made in the current work, where the void density and total area fraction was higher in the finer martensite TMC4 microstructure, compared to the TMC5 microstructure, where voids grew along the bainite grains.

Qualitatively, void growth appears to be higher for TMC4 as shown by the large voids in Figures 18(a) and (b) (right-hand side void only). These voids are not associated with TiN particles and appear to have nucleated at martensite/bainite interfaces and grown (and/or coalesced) in the loading direction. This mode was observed in all of the images presented in Figure 18. Long and coalesced voids, which develop due to "necklace" coalescence,[50] were observed for TMC4 (Figure 18(d)) at a low thickness strain. This is supported by the high void area fraction for TMC4 at 0.20 thickness strain when compared to the other material conditions in Figure 12(b). Also, void density is greatest for this tailored material conditions as shown in Figure 12(b). To a lesser extent, necklacing coalescence was also observed in TMC5 (Figure 19(d)). EDX analysis of these voids did not detect the presence of non-metallic inclusions.

TiN particles contribute significantly to the total void accumulation of TMC4 (Figure 18(b)), but to a lesser extent for TMC5 (Figure 19(c)) as shown in Figure 11. The greater strength differential between martensite/bainite and the higher volume fraction of bainite in TMC4 possibly contributed to the observed phenomenon.

It should be noted that the triaxiality within the neck of the TMC4 specimen was different due to the 1.8 mm thickness of this sheet, rather than 1.2 mm. This effect was not quantified in the current work.

7. *MART damage characterization*

The measured void accumulation for this fully martensitic material condition is lower than all of the tailored material conditions examined in this work. This is somewhat counter intuitive, considering the low ductility (total elongation) and low percent area reduction as shown in Figure 5(d). Zhang *et al.*[51] have shown that a hot stamped steel does undergo ductile fracture. At the highest thickness strain level, near the fracture surface (Figure 15(e)), the observed number of voids is minimal, which is supported by the low measured void density. Figure 15(e) shows the highly deformed and aligned martensitic grains near the fracture surface and with the absence of a soft phase to promote decohesion, void nucleation appears to have been suppressed, but a shear fracture surface was observed. Landron *et al.*[52] conducted *in-situ* tensile tests on DP and martensitic steel specimens with X-ray microtomography imaging. They showed that void growth was greater for the martensitic steel at high strain levels, near the fracture surface. This suggests that a small number of very large voids could contribute to the final and catastrophic fracture for this material condition.

The carbon content of this martensite is that of the base material (0.22 wt pct) which is the lowest of all the tailored material conditions considered in this work. It was observed that many of the measured voids typically nucleated at TiN particles as shown in Figures 20(b) and (d). Similar to TMC4 and TMC5, necklacing coalescence was detected in this material as shown in Figure 20(c) (inclusion free *via* EDX analysis).

IV. CONCLUSIONS

Based on the results presented in this article, the following conclusions can be made:

1. The tensile properties of the tailored microstructures revealed that in-die heating temperatures of 600 °C and 700 °C developed tailored microstructures with an excellent balance of strength and ductility, making them suitable for implementation within tailor hot stamped energy absorbing structure. In particular, the 700 °C tailored material condition (TMC1), exhibited a hardness of 192 HV_{1000}, a tensile strength of 615 MPa, and a total elongation of 0.24. At the other end of the tailored material condition spectrum, TMC3, created using a die temperature of 400 °C resulted in a tailored material condition with intermediate tensile strength and a relatively low (and less desirable) total elongation of 842 MPa and 0.11, respectively.

2. Microstructural analysis revealed that a large variation in multi-phase composition can be developed using the in-die heating tailoring technique. The high die temperatures (600 °C and 700 °C) produce a predominantly pearlitic/ferritic microstructure, with some martensite. For hot stamping die temperatures of 400 °C, the variation in multi-phase microstructures varied in composition with different volume fractions of ferrite, martensite, and 2 variants of bainite as shown for TMC3 to TMC5. It was also shown that these tailored material conditions were susceptible to martensite formation at grain boundaries and grain boundary junctions.

3. With respect to damage evolution, the void area fractions of TMC1 and TMC2 are different, even though their mechanical properties and microstructures are somewhat similar. The higher strength and greater void accumulation of TMC2 can be attributed to a more refined microstructure and increased martensite area fraction, especially at grain boundaries and grain boundary junctions. The dominant nucleation modes for these two material conditions were associated with martensite particle cracking, separation, and decohesion from the softer phases.

4. The bainitic (B1 and B2 variants), martensitic, and ferritic multi-phase microstructure of TMC3 resulted in the highest void accumulation and measured void density among the material conditions examined in this work. Void characterization revealed that the martensite formed at the grain boundaries and grain boundary junctions acted as nucleation sites, resulting in poor damage performance.

5. The predominantly bainitic material conditions with increasing area fractions of martensite (TMC4 to MART) revealed a decrease in void accumulation for increasing martensitic area fractions. This was a result of the reduction in martensite strength for increasing area fractions of martensite in the microstructure, as well as the reduction in area fraction of the softer bainitic phase. Necklacing coalescence was observed for this class of tailored material conditions.

6. TiN particles contributed negatively to the damage accumulation for all of the material conditions. It was shown that TMC3 and TMC4 were the most susceptible to increased void accumulation due to the presence TiN particles.

REFERENCES

1. H. Karbasian and E. Tekkaya: *J. Mater. Process. Technol.*, 2010, vol. 210, pp. 2103–18.
2. M. Maikranz-Valentin, U. Weidig, U. Schoof, H.H. Becker, and K. Steinhoff: *Steel Res. Int.*, 2008, vol. 79, pp. 92–97.
3. M. Merklein, M. Wieland, M. Lechner, S. Bruschi, and A. Ghotti: *J. Mater. Process. Technol.*, 2016, vol. 228, pp. 11–24.
4. R. George, A. Bardelcik, and M.J. Worswick: *J. Mater. Process. Technol.*, 2012, vol. 212, pp. 2386–99.
5. B. Klein, S. Crichley, and K. Khang: *Great Designs in Steel Seminar*, Livonia, Michigan, 2015.
6. A. Bardelcik, C. Salisbury, S. Winkler, M.J. Worswick, and M. Wells: *Int. J. Impact Eng.*, 2010, vol. 37, pp. 694–702.
7. A. Bardelcik, M.J. Worswick, S. Winkler, and M. Wells: *Int. J. Impact Eng.*, 2012, vol. 50, pp. 49–62.
8. A. Barcellona and D. Palmeri: *Metall. Mater. Trans. A.*, 2009, vol. 40A, pp. 1160–74.
9. J. Min, J. Lin, Y. Min, and F. Li: *Mater. Sci. Eng. A.*, 2012, vol. 550, pp. 375–87.
10. A. Bardelcik, M.J. Worswick, and M. Wells: *Mater. Des.*, 2014, vol. 55, pp. 509–25.
11. S. Golling, R. Ostlund, and M. Oldenburg: *J. Mater. Process. Technol.*, 2016, vol. 228, pp. 88–97.
12. P. Srithananan, P. Kaewtatip, and V. Uthaisangsuk: *Mat. Sci. Eng. A.*, 2016, vol. 667, pp. 61–76.
13. B.T. Tang, Q.L. Wang, S. Bruschi, A. Ghiotti, and P.F. Bariani: *J. Manuf. Sci. E-T ASME*, 2014, vol. 136, pp. 1–14.
14. T.K. Eller, L. Greve, M. Andres, M. Medricky, V.T. Meinders, and A.H. van den Boogaard: *J. Mater. Process. Technol.*, 2016, vol. 228, pp. 43–58.
15. T.K. Eller, L. Greve, M. Andres, M. Medricky, A. Hatscher, V.T. Meinders, and A.H. van den Boogaard: *J. Mater. Process. Technol.*, 2014, vol. 214, pp. 1211–27.
16. D. Mohr and F. Ebnoether: *Int. J. Solids Struct.*, 2009, vol. 46, pp. 3535–47.
17. K. Omer, L. ten Kortenaar, C. Butcher, M.J. Worswick, S. Malcolm, and D. Detwiler: *Int. J. Impact Eng.*, 2017, vol. 103, pp. 12–28.
18. Y. Prajogo: MASc Thesis, University of Waterloo, 2015.

19. K. Omer, R. George, A. Bardelcik, M.J. Worswick, S. Malcolm, and D. Detwiler: *Int. J. Mater. Form.*, 2018, vol. 11 (1), pp. 149–64.
20. ArcelorMittal – Usibor® 1500-AS CCT diagram (personal communication), 2009.
21. R. Smerd, S. Winkler, C. Salisbury, M. Worswick, D. Lloyd, and M. Finn: *Int. J. Impact Eng.*, 2005, vol. 32, pp. 541–60.
22. G. Krauss: *Mat. Sci. Eng. A.*, 1999, vols. A273–275, pp. 40–57.
23. T.N Baker: *Mater. Sci. Technol.* 2009, vol. 25, pp. 1083-107.
24. Y. Li and T.N. Baker: *Mat. Sci. Technol.*, 2010, vol. 26, pp. 1029–40.
25. N. Huda, A.R.H. Midawi, J. Gianetto, R. Lazor, and A.P. Gerlich: *Mater. Sci. Eng. A.*, 2016, vol. 662, pp. 481–91.
26. H.C. Chen and G.H. Cheng: *J. Mater. Sci.*, 1989, vol. 24, pp. 1991–94.
27. H.K.D.H. Bhadeshia and D.V. Edmonds: *Met. Sci.*, 1983, vol. 17, pp. 411–19.
28. M.X. Zhang and P.M. Kelly: *Mater. Char.*, 1998, vol. 40, pp. 159–68.
29. K. Banjerjee: *Int. J. Metall. Eng.*, 2013, vol. 2 (1), pp. 100–10.
30. H.K.D.H. Bhadeshia and J.W. Christian: *Metall. Mater. Trans. A.*, 1990, vol. 21A, pp. 769–97.
31. F.G. Caballero, H. Roelofs, S. Hasler, C. Capdevila, J. Chao, J. Cornide, and C. Garcia-Mateo: *Mater. Sci. Technol.*, 2012, vol. 28, pp. 95–102.
32. T. Furuhara, H. Kawata, S. Morito, and T. Maki: *Mater. Sci. Eng. A.*, 2006, vol. 431, pp. 228–36.
33. G. Krauss: *Principles of Heat Treatment of Steel*, 1st ed., American Society for Metals, Metals Park, 1980.
34. H. Jarvinen, M. Isakov, T. Nyyssonen, M. Jarvenpaa, and P. Peura: *Mater. Sci. Eng. A.*, 2016, vol. 676, pp. 109–20.
35. B. Abrivard, E. Pessard, F.M.P. Delhaye, and B. Gerin: *13th International Spring Meeting SF2M*, May 22-23, Paris, France, 2013.
36. D.K. Matlock and J.G. Speer: *Mater. Sci. Technol.*, 2009, vol. 25, pp. 1118–25.
37. S. Vervynckt, K. Verbeken, B. Lopez, and J.J. Jonas: *Int. Mater. Rev.*, 2012, vol. 57, pp. 187–207.
38. H. Scott, J.D. Boyd, and A.K. Pilkey: *Mater. Sci. Eng. A.*, 2017, vol. 682, pp. 139–46.
39. N. Pathak, C. Butcher, M.J. Worswick, E. Bellhouse, and J. Gao: *Materials*, 2017, vol. 10, pp. 1–29.
40. Q. Lai, O. Bouaziz, M. Goune, L. Brassart, M. Verdier, G. Parry, A. Perlade, Y. Brecht, and T. Pardoen: *Mater. Sci. Eng. A.*, 2015, vol. 646, pp. 322–31.
41. G. Avramovic-Cingara, A.R. Saleh, M.K. Jain, and D.S. Wilkinson: *Metall. Mater. Trans. A.*, 2009, vol. 40A, pp. 3117–27.
42. J. Kadhodapour, A. Butz, and S. Ziaei Rad: *Acta Mater.*, 2011, vol. 59, pp. 2575–88.
43. A.F. Szewczyk and J. Gurland: *Metall. Trans. A.*, 1982, vol. 13A, pp. 1821–26.
44. E. Maire, O. Bouaziz, M. Di Michiel, and C. Verdu: *Acta Mater.*, 2008, vol. 56, pp. 4954–64.
45. J. Samei, D.G. Green, J. Cheng, and M.S. Lima: *Mater. Des.*, 2016, vol. 92, pp. 1028–37.
46. C.I.A. Thomson, M.J. Worswick, A.K. Pilkey, and D.J. Lloyd: *J. Mech. Phys. Solids*, 2003, vol. 51, pp. 127–46.
47. M. Erdogan: *J. Mater. Sci.*, 2002, vol. 37, pp. 3623–30.
48. M. Azuma, S. Goutianos, N. Hansen, G. Winther, and X. Huang: *Mater. Sci. Technol.*, 2012, vol. 28 (9–10), pp. 1092–100.
49. N.J. Kim and G. Thomas: *Metall. Mater. Trans. A.*, 1981, vol. 12A, pp. 483–89.
50. A.A. Benzerga: PhD Thesis, Ecole National Superieure des Mines de Paris, 2000.
51. S. Zhang, Y. Huang, B. Sun, Q. Liao, H. Lu, B. Jian, H. Mohrbacher, W. Zhang, A. Guo, and Y. Zhang: *Mater. Sci. Eng. A.*, 2015, vol. 626, pp. 136–43.
52. C. Landron, E. Maire, O. Bouaziz, J. Adrien, L. Lecarme, and A. Bareggi: *Acta Mater.*, 2011, vol. 59, pp. 7564–73.